C. R. Mecanique 343 (2015) 443–456

Contents lists available at ScienceDirect

Comptes Rendus Mecanique

www.sciencedirect.com

An identification method to calibrate higher-order parameters in local second-gradient models

Méthode d'identification des paramètres d'ordre supérieur dans les modèles second gradient locaux

Simon Raude [a], Richard Giot [a,*], Alexandre Foucault [b], Roméo Fernandes [b]

[a] *GeoRessources, UMR 7359 ENSG–Université de Lorraine, 54518 Vandœuvre-lès-Nancy, France*
[b] *IMSIA, UMR EDF-CNRS-CEA-ENSTA 9219, Clamart, France*

ARTICLE INFO

Article history:
Received 31 October 2014
Accepted 10 June 2015
Available online 3 July 2015

Keywords:
Second-gradient dilation model
Localisation
Material property identification
Shear bands
3-D modelling
Softening behaviour

Mots-clés :
Modèles second gradient de dilatation
Localisation
Identification des propriétés des matériaux
Bandes de cisaillement
Modélisation 3D
Radoucissement

ABSTRACT

A numerical method is presented for identifying the material parameters that appear in second-gradient models. For local second-gradient models, additional material parameters must be defined in numerical models. The objective of the present study is to develop a simple numerical identification procedure for these additional coefficients. The method combines modelling of laboratory tests with analytical implements. Numerical studies are then used to validate the method for a shale and to investigate the effects of both the internal length and the additional coefficients on the numerical responses. The procedure provides the first coherent results achieved at the laboratory scale.

RÉSUMÉ

Une méthode numérique permettant d'identifier les paramètres matériaux spécifiques aux modèles second gradient est présentée. Pour les modèles second gradient locaux, des paramètres matériaux supplémentaires sont définis dans les modèles numériques. L'objectif est de développer une procédure d'identification numérique simple pour ces coefficients supplémentaires. La méthode combine la modélisation d'essais de laboratoire et des développements analytiques. Des études numériques permettent de valider la méthode sur une argile et d'investiguer les effets de la longueur interne et des coefficients supplémentaires sur la réponse numérique. La procédure fournit les premiers résultats cohérents à l'échelle du laboratoire.

* Corresponding author at: GeoRessources, UMR 7359 ENSG–Université de Lorraine, 2, rue du Doyen-Marcel-Roubault – TSA 70605, 54518 Vandœuvre-les-Nancy cedex, France. Tel.: +33 3 83 59 63 17; fax: +33 3 83 59 63 00.
E-mail addresses: simon.raude@edf.fr (S. Raude), richard.giot@univ-lorraine.fr (R. Giot), Alexandre.Foucault@edf.fr (A. Foucault), romeo.fernandes@edf.fr (R. Fernandes).

http://dx.doi.org/10.1016/j.crme.2015.06.002
1631-0721/

1. Introduction

Geomaterials exhibit multi-scale behaviour, which results from their heterogeneous structure of minerals, matrix, cracks, and pores. This specific structure leads to complex pressure-dependent mechanical responses and the frequent occurrence of localised deformation phenomena [1,2]. In the last few decades, a number of theoretical approaches have been developed to describe the mechanics of these materials. Examples include higher-order continuum methods, multi-scale approaches using homogenisation, and discrete element methods. In this study, we use the first of these approaches to solve strain localisation problems encountered in modelling the behaviour of geomaterials.

Strain localisation is an important phenomenon that occurs in all types of materials, including metals, polymers and geomaterials. The phenomenon is particularly problematic when modelling strain softening in geomaterials using classical constitutive equations. These equations are known to produce non-dissipative numerical solutions [3] with mesh dependencies (in terms of the size and the orientation) [4,5] as well as strain localisation in thin zones known as shear bands. While these constitutive equations may be able to predict the occurrence of strain localisation [6,7], they cannot be used to describe the localised states [5]. Hence, they must be modified by integrating an implicit internal length for modelling strain localisation [8,9].

Following the pioneering works of Aifantis [9–11], a number of enhanced constitutive equations have been developed for modelling localised zones. These models can be grouped into three categories: non-local models (see Bazant [3], for instance), which have been mainly applied to concrete; gradient plasticity models [12,13], which have been used for a variety of materials; and models derived for Cosserat materials, which are based on micro-structure media theory (also called micro-morphic media theory) [14–16], and which have generally been used for describing geomaterials.

Chambon et al. [17,18] developed local second-gradient models by introducing additional mathematical constraints to link the micro and macro quantities involved in the micro-morphic media framework. In addition to the classical displacement field, an enhanced kinematical variable and additional constitutive equations must also be included in these models. A second order field is generally introduced for strains and rotations of the grains at a micro-scale. Although this approach facilitates precise description of micro-scale phenomena in geomaterials, the localisation computations are often very time-consuming and are difficult to complete for large-scale applications. The present study mainly focuses on the laboratory (specimen) scale, with the aim of eventually extending the results to industrial cases. It is therefore necessary to consider simplified enhancements. The strong volume changes that occur in most geomaterials during the development of shear bands (e.g., [19–21]) have led to the development of models that involve volumetric quantities (e.g., [22,23]). In these models, the enhanced kinematical variable is a scalar (instead of a complete second-order tensor). This clearly reduces the number of degrees of freedom and thus the time required for the localisation computations. Note, however, that this type of theory is unsuitable for materials that do not exhibit volume changes during plastic loading. In this paper, we work within the framework of the second-gradient dilation model developed by Fernandes et al. [23].

In computational mechanics, the material parameters in classical constitutive equations (used in computations involving classical kinematics) are usually calibrated using experimental laboratory tests that are traditionally used for modelling large-scale phenomena (such as tunnel excavations and the behaviour of dams and concrete structures; see [24–26], for example). The use of higher order terms for modelling strain localisation requires the definition of additional coefficients and the use of a specific calibration procedure for identifying these material properties. Unfortunately, it is not always possible to obtain data for enhanced models from traditional experimental methods, which probe the macro-scale response of materials and not their internal structure and deformation mechanisms (shear-band development, the kinematics of individual grains and the distribution of the force-transmitting contacts). The development of specific laboratory tests for the calibration of higher order parameters is a critical initiative that is still in progress [1,2,21].

In order to identify shear band thickness, these parameters must be assessed by measurement at a local scale rather than at the more standard sample scale. Different methods have been proposed, among them False Relief Sterophotogrammetry (FRS) and Computed X-ray Tomography [27]. The main drawback of the latter is its inefficiency to capture deformation in the absence of changes in material density, i.e. in the absence of variations in volume. To overcome this limitation, CT X-ray has been coupled to 3D Volumetric Digital Image Correlation (DIC) for application to clay rock and granular material [28]. Nevertheless, the number of in situ tomography tests remains limited and the resolution of conventional CT systems restricts their practical use to coarse-grained materials such as sand. For fine-grained materials such as claystone or shale, the shear bands are thinner and their measurement requires a higher resolution, which can only be achieved with more powerful, but less widely available, X-ray sources [28].

Our objective here, however, is to develop a simple numerical identification procedure that combines traditional modelling tests with theoretical implements. The modelling tests enable the classical material constants to be calibrated and the analytical results are then used to identify the higher order parameters. The effect of these additional quantities on the width of the shear bands in the localised regime is well known, as is the reciprocal influence of this width on the stress–strain relationship [29]. These parameters are directly related to the implicit internal length introduced by the corresponding second-gradient model. In simple cases, the analytical solutions of 1-D boundary value problems can be used to provide an explicit relationship between these parameters and the implicit internal length [30,31]. The additional parameters can be derived by making geometrical assumptions about the implicit internal length.

It should be noted that mesh effects are not directly addressed in this study. In our experience, however, we have found that a minimum of four or five elements are required to model the width of the shear bands in order to obtain

mesh-independent results [23,29]. This number of elements ensures an accurate description of localisation for the various applications considered in this study. This assumption may also be used to estimate the implicit internal length, an input which is required for deriving the additional coefficients.

In the first part of this paper, we present the main notations. For clarity, tensors and vectors are presented in terms of their components, which are identified by lowercase subscripts. Exponents or upper-case subscripts have different meanings here. Repeated indices indicate the summation convention for tensors. In the second section, we present the context of our study by discussing the general theoretical considerations. The key developments in the second-gradient dilation model are reviewed first, followed by a discussion of the constitutive equations. The constitutive equation used here is a straightforward extension of an elastoplastic softening Drucker–Prager model that involves an implicit internal length. We then go on to solve a simple boundary value problem in order to illustrate how the theoretical implements can be used to estimate the higher order parameters. We then describe the identification procedure and, in the section that follows, we use different applications to validate the method and to discuss the effects of the implicit internal length and the extra coefficients on the numerical responses. The experimental data are briefly presented first, followed by the numerical applications. The finite element open source software *Code_Aster* [32] is used to perform the computations. The paper ends with concluding remarks and a discussion of future work.

2. Theoretical considerations

In this section, we present the preliminary theoretical considerations and review the background to the theory in order to outline the context of the present study. First, the second-gradient dilation model is mathematically formulated, and we discuss its relationship to the second gradient model and the microdilation model. Next, we introduce the constitutive equations. The underlying first gradient model corresponds to an elastoplastic softening Drucker–Prager model [34], which has been enhanced using concepts developed by Mindlin [15]. A simple boundary value problem is then solved to illustrate how the analytical results can be used to estimate the higher order coefficients.

2.1. Second gradient dilation model

The second-gradient dilation model can be viewed as either a constrained micromorphic dilation model [22] or as a simplified local second-gradient model [30]. The similarities between these two models can be seen by examining the governing equations chronologically, from the initial micromorphic models to the second-gradient model and up to the more recently developed microdilation model.

In micromorphic models, an enhanced kinematics must be defined in addition to the classical displacement field, denoted by u_i. A second order field, known as a micro deformation gradient and denoted by f_{ij}, is typically introduced to model the strains and the rotations of the grains at the micro-scale. Note that, unlike the classical deformation field, this micro deformation gradient is not the gradient of an underlying displacement field. Neglecting the body forces (for simplicity) and taking into account the higher order terms, the principle of virtual work thus yields the following result for arbitrary kinematically admissible fields (u_i^*, f_{ij}^*) where u_i^* and f_{ij}^* are sufficiently smooth and have null values on the parts of the boundary where the corresponding real field is prescribed:

$$\int_\Omega \left(\sigma_{ij} \frac{\partial u_i^*}{\partial x_j} + \tau_{ij} \left(f_{ij}^* - \frac{\partial u_i^*}{\partial x_j} \right) + \Sigma_{ijk} \frac{\partial f_{ij}^*}{\partial x_k} \right) \mathrm{d}v = \int_{\partial\Omega} \left(t_i u_i^* + T_{ij} f_{ij}^* \right) \mathrm{d}s \tag{1}$$

where σ_{ij}, τ_{ij} and Σ_{ijk} are the macro-stress, micro-stress and the double stress tensors, respectively. The traction forces t_i and the double surface tractions T_{ij} are prescribed on the boundary $\partial\Omega$. x_j are the coordinates for an orthonormal Cartesian basis.

Kinematic constraints can be added to the previous formulation by forcing the micro gradient to equal the macro gradient: $f_{ij}^* = \frac{\partial u_i^*}{\partial x_j}$. This constraint produces the second-gradient model [30]. The equation for the principle of virtual work for a kinematically admissible field u_i^* can be expressed as

$$\int_\Omega \left(\sigma_{ij} \frac{\partial u_i^*}{\partial x_j} + \Sigma_{ijk} \frac{\partial^2 u_i^*}{\partial x_j \partial x_k} \right) \mathrm{d}v = \int_{\partial\Omega} \left(p_i u_i^* + P_i D u_i^* \right) \mathrm{d}s \tag{2}$$

where p_i and P_i are the force per unit area and the additional external (double) force per unit area, respectively. For conciseness, these forces are not detailed in the present paper. In Equations (1) and (2), the micro deformation gradient f_{ij} triggers the appearance of an implicit internal length in these models. However, this enhanced kinematics introduces many additional degrees of freedom to the corresponding finite element formulation. Microdilation media [22] possess all the advantages of micromorphic models, but the number of degrees of freedom is reduced through the introduction of only volumetric quantities. In these cases, the enhanced kinematical variable χ corresponds to the microvolume change and its gradient. The classical stress field σ_{ij} is augmented by introducing the micro dilation stress, which is denoted by κ, and the

double dilation stresses, denoted by S_j. Applying the principle of virtual work to a kinematically admissible field (u_i^*, χ^*) yields:

$$\int_\Omega \left(\sigma_{ij} \frac{\partial u_i^*}{\partial x_j} + \kappa \left(\epsilon_V^* - \chi^* \right) + S_j \frac{\partial \chi^*}{\partial x_j} \right) \mathrm{d}v = \int_{\partial\Omega} \left(t_i u_i^* + m\chi^* \right) \mathrm{d}s \tag{3}$$

For conciseness, the boundary conditions t_i and m are not detailed in this paper. In the same way that the micromorphic model was transformed to the second-gradient model, a kinematic constraint can be introduced between the macro volume change ϵ_V^* and the microdilation χ^*. This modification produces the second-gradient dilation model [23]. We thus obtain the following equation for a kinematically admissible displacement field u_i^*:

$$\int_\Omega \left(\sigma_{ij} \frac{\partial u_i^*}{\partial x_j} + S_j \frac{\partial^2 u_i^*}{\partial x_i \partial x_j} \right) \mathrm{d}v = \int_{\partial\Omega} \left(p_i u_i^* + P_i D u_i^* \right) \mathrm{d}s \tag{4}$$

where p_i and P_i are boundary conditions given by

$$\begin{cases} p_i = \sigma_{ij} n_j - n_i n_j D S_j - \dfrac{D S_j}{D x_j} n_i - \dfrac{D S_j n_j}{D x_i} + \dfrac{D n_p}{D x_p} S_j n_j n_i \\ P_i = S_j n_j n_i \end{cases} \tag{5}$$

In this equation, n_j are the components of the unit outward normal to a boundary. For simplicity, we assume that $P_i = 0$. Boundary conditions that prescribe a non-zero value of P_i will in general only induce effects such as boundary layers in the vicinity of the boundaries. However, in this paper, we are mainly interested in the phenomenon of localisation. The aforementioned assumption results in $S_j n_j = 0$ on the requisite section of the boundary (see [23,29,30]). In this case, Equation (5) reduces to:

$$\begin{cases} p_i = \sigma_{ij} n_j - \dfrac{\partial S_j}{\partial x_j} n_i \\ P_i = 0 \end{cases} \tag{6}$$

The strong form of the virtual work principle (the balance equation) can be written as:

$$\frac{\partial \sigma_{ij}}{\partial x_j} - \frac{\partial^2 S_j}{\partial x_i \partial x_j} = 0 \tag{7}$$

As mentioned by Fernandes et al. [23], the main limitation of the second-gradient dilation model is that regularizing effects are brought about only by changes in volume. As a result, the efficiency of the model is limited to loading conditions that involve volume changes, dilatancy or contractancy. Simulations of pure shear bands will be mesh-dependent according to this approach. An alternative approach would be a micromorphic model, or its gradient limit, based on the total equivalent strain, or equivalent/cumulative plastic strain, instead of only the dilation [30]. However, an approach such as this is difficult and cumbersome to implement. The second-gradient dilation model is not suitable for materials that do not exhibit volume changes during plastic loading. Nevertheless, for geomaterials, large deformations in localized zones are generally accompanied by volume changes, due to either the enlargement of voids in soils or the development of micro fractures in rocks and concrete [33,27]. In claystones, however, volume changes may be relatively limited compared to shear strains [28].

Concerning the numerical formulation and implementation, details can be found in [23]. Implementation of Equation (4) in the finite element code *Code_Aster* (Edf) requires the definition of new finite elements that allow the continuity of ϵ_V^* to be enforced through Lagrange multipliers. The additional field χ was added and the equality between the micro and macro dilations $\epsilon_V^* = \chi$ was enforced using a Lagrange multiplier field Ξ. A penalization term, r, was also introduced in which r is an elastic constant. Finally, the virtual work Equation (4) can be rewritten in the form:

$$\int_\Omega \left(\sigma_{ij} \epsilon_{ij}^* + S_j \frac{\partial \chi^*}{\partial x_j} - \Xi(\epsilon_V^* - \chi^*) + \Xi^*(\epsilon_V - \chi) + r(\epsilon_V - \chi)(\epsilon_V^* - \chi^*) \right) \mathrm{d}v = \int_{\partial\Omega} \left(p_i u_i^* + P_i D u_i^* \right) \mathrm{d}s \tag{8}$$

which must be verified for any kinematic admissible fields (u_i^*, χ^*, Ξ^*). Several finite elements were developed with different finite element interpolations. u_i and χ are discretized by polynomial functions of two and one degrees, respectively, and are continuous from one element to the adjacent ones. Several shape functions for the Lagrange multipliers Ξ are implemented: constant, and first and second orders. The balanced equation is written in a weak form and discretized using a finite element method. This yields a set of non-linear equations that are then solved with a Newton–Raphson method.

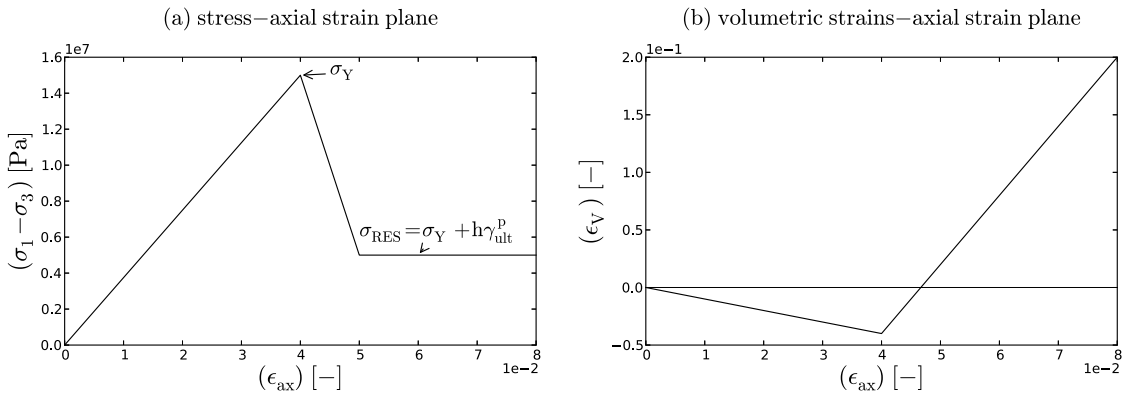

Fig. 1. Typical responses in standard homogeneous triaxial tests.

2.2. Constitutive equations

Equations (6) and (7) demonstrate the need to define constitutive equations. The procedure detailed in Section 3, below, is applied to a shale material in Section 4. A common way to model strain softening in geomaterials is to decrease the cohesion forces with increasingly plastic behaviour of the material. In this study, the decrease is modelled using the Drucker–Prager associated plasticity approach [34]. Though the model may appear too simplistic for accurate description of both strain softening phenomena and the volume changes that occur in geomaterials, the aim of this study is to develop an identification procedure that can later be used with any constitutive model. In the following section, the corresponding constitutive equations are first briefly reviewed. A linear isotropic elastic model based on the work of Mindlin [15] is assumed for the second-gradient component. The corresponding equations are then presented in the section that follows.

2.2.1. Drucker–Prager constitutive equations

The yield condition is expressed by:

$$F(\boldsymbol{\sigma}, \gamma^p) = \sqrt{3J_2} + \alpha I_1 - R(\gamma^p)$$
$$I_1 = \sigma_{ij}\delta_{ji} \qquad J_2 = \frac{1}{2}s_{ij}s_{ji} \tag{9}$$

In these equations, s_{ij} are the components of the deviatoric macro-stress tensor and δ_{ij} are the components of the identity tensor. α is a material parameter that is related to the friction angle ϕ (Equation (11)). The function $R(\gamma^p)$ induces strain softening through the deterioration of cohesion, which is a common way of modelling failure in soft rocks. We assume that $R(\gamma^p)$ is linear from the peak strength ($\gamma^p = 0$) to the residual strength ($\gamma^p = \gamma^p_{ult}$) (see Fig. 1 and Equation (10)):

$$\begin{cases} R(\gamma^p) = \sigma_Y + h\gamma^p & \text{if } \gamma^p \in [0,\ \gamma^p_{ult}] \\ R(\gamma^p) = \sigma_Y + h\gamma^p_{ult} & \text{if } \gamma^p > \gamma^p_{ult} \end{cases} \tag{10}$$

where σ_Y is a parameter from which the cohesion coefficient C can be derived (see Equation (11)). The slope of the softening branch is given by h (see Fig. 1). The accumulated plastic distortion γ^p, as defined by Equation (12), is the internal state variable in the model. The variable γ^p_{ult} signals the transition towards the residual threshold (see Fig. 1a).

$$\begin{cases} \alpha = \dfrac{2\sin(\phi)}{3 - \sin(\phi)} \\ \sigma_Y = \dfrac{6C\cos(\phi)}{3 - \sin(\phi)} \end{cases} \tag{11}$$

$$\gamma^p = \int_0^t \left(\frac{2}{3}\dot{e}^p_{ij}\dot{e}^p_{ij}\right)^{\frac{1}{2}} \mathrm{d}t \tag{12}$$

where e^p_{ij} are the components of the deviatoric plastic macro-strain tensor. Fig. 1 illustrates typical responses in standard homogeneous triaxial testing, both in the stress-axial strain plane (Fig. 1a) and in the volumetric strain-axial strain plane (Fig. 1b).

After linear elastic loading, the response is characterized by a linear strain softening followed by a plateau (Fig. 1a). After an initial decrease in the volumetric strains up to the peak strength, the volumetric strains are seen to increase (Fig. 1b). This increase is continued because the model is associative.

The plastic strain rate is obtained by applying the normality rule, which introduces the plastic multiplier $\dot{\lambda}$, which is a positive scalar associated with the loading-unloading condition from the Kuhn–Tucker complementary conditions. As we consider a Drucker–Prager associated model, the plastic potential is equal to the yield function (9). The stress state must satisfy the *persistency* (or *consistency*) condition. The constitutive equations can thus be expressed as a rate as:

$$\dot{\sigma}_{ij} = \Lambda^{\mathrm{ep}}_{ijkl}\dot{\epsilon}_{lk} \tag{13}$$

where ϵ_{ij} are the components of the macro-strain tensor and $\Lambda^{\mathrm{ep}}_{ijkl}$ is the fourth order tangent elasto-plastic tensor given by:

$$\Lambda^{\mathrm{ep}}_{ijkl} = \Lambda^{\mathrm{e}}_{ijkl} - \frac{\Lambda^{\mathrm{e}}_{ijmn}G_{nm}G_{op}\Lambda^{\mathrm{e}}_{pokl}}{G_{qr}\Lambda^{\mathrm{e}}_{rqst}G_{ts} - L} \tag{14}$$

G_{ij} and L are defined by:

$$G_{ij} = \frac{\partial F}{\partial \sigma_{ij}} \quad ; \quad L = \sqrt{\frac{2}{3}}\frac{\partial F}{\partial \gamma^{\mathrm{p}}}\tilde{G}_{II} \quad ; \quad \tilde{G}_{II} = \sqrt{\tilde{G}_{ij}\tilde{G}_{ji}} \quad ; \quad \tilde{G}_{ij} = G_{ij} - \frac{G_{kk}}{3}\delta_{ij} \tag{15}$$

where $\Lambda^{\mathrm{e}}_{ijkl}$ is the fourth order elastic stiffness tensor. The rate forms of the classical constitutive equations can be written as:

$$\begin{bmatrix} \dot{\sigma}_{11} \\ \dot{\sigma}_{22} \\ \dot{\sigma}_{12} \\ \dot{\sigma}_{21} \end{bmatrix} = \begin{bmatrix} \Lambda^{\mathrm{ep}}_{1111} & \Lambda^{\mathrm{ep}}_{1122} & \Lambda^{\mathrm{ep}}_{1112} & \Lambda^{\mathrm{ep}}_{1121} \\ \Lambda^{\mathrm{ep}}_{2211} & \Lambda^{\mathrm{ep}}_{2222} & \Lambda^{\mathrm{ep}}_{2212} & \Lambda^{\mathrm{ep}}_{2221} \\ \Lambda^{\mathrm{ep}}_{1211} & \Lambda^{\mathrm{ep}}_{1222} & \Lambda^{\mathrm{ep}}_{1212} & \Lambda^{\mathrm{ep}}_{1221} \\ \Lambda^{\mathrm{ep}}_{2111} & \Lambda^{\mathrm{ep}}_{2122} & \Lambda^{\mathrm{ep}}_{2112} & \Lambda^{\mathrm{ep}}_{2121} \end{bmatrix} \begin{bmatrix} \dot{\epsilon}_{11} \\ \dot{\epsilon}_{22} \\ \dot{\epsilon}_{12} \\ \dot{\epsilon}_{21} \end{bmatrix} \tag{16}$$

Note that the tangent elasto-plastic tensor is symmetric because the model is associative. The tangent elasto-plastic tensor components are detailed in Equation (17) and will be applied in Section 2.3 below.

$$\begin{cases} \Lambda^{\mathrm{ep}}_{1111} = \left(K + \frac{4}{3}G\right) - \frac{4}{H}\left(\alpha\left(K + \frac{G}{3}\right) + G\left(\frac{\sigma_{11}-\sigma_{22}}{2\tau}\right)\right)^2 \\ \Lambda^{\mathrm{ep}}_{1122} = \Lambda^{\mathrm{ep}}_{2211} = \left(K - \frac{2}{3}G\right) - \frac{4}{H}\left(\alpha^2\left(K + \frac{G}{3}\right)^2 - G^2\left(\frac{\sigma_{11}-\sigma_{22}}{2\tau}\right)^2\right) \\ \Lambda^{\mathrm{ep}}_{1112} = \Lambda^{\mathrm{ep}}_{1121} = \Lambda^{\mathrm{ep}}_{1211} = \Lambda^{\mathrm{ep}}_{2111} = -\frac{1}{H}\left(\frac{4G\sigma_{12}}{\tau}\right)\left(\alpha\left(K + \frac{G}{3}\right) + G\left(\frac{\sigma_{11}-\sigma_{22}}{2\tau}\right)\right) \\ \Lambda^{\mathrm{ep}}_{2222} = \left(K + \frac{4}{3}G\right) - \frac{4}{H}\left(\alpha\left(K + \frac{G}{3}\right) - G\left(\frac{\sigma_{11}-\sigma_{22}}{2\tau}\right)\right)^2 \\ \Lambda^{\mathrm{ep}}_{2212} = \Lambda^{\mathrm{ep}}_{2221} = \Lambda^{\mathrm{ep}}_{1222} = \Lambda^{\mathrm{ep}}_{2122} = -\frac{1}{H}\left(\frac{4G\sigma_{12}}{\tau}\right)\left(\alpha\left(K + \frac{G}{3}\right) - G\left(\frac{\sigma_{11}-\sigma_{22}}{2\tau}\right)\right) \\ \Lambda^{\mathrm{ep}}_{1212} = \Lambda^{\mathrm{ep}}_{1221} = \Lambda^{\mathrm{ep}}_{2121} = \Lambda^{\mathrm{ep}}_{2112} = G - \frac{1}{H}\left(\frac{2G\sigma_{12}}{\tau}\right)^2 \end{cases} \tag{17}$$

where K and G are the bulk and shear moduli, respectively, $H = \left(G_{qr}\Lambda^{\mathrm{e}}_{rqst}G_{ts} - L\right)$ equals the denominator in Equation (14), and $-L$ is the standard hardening modulus defined by:

$$\begin{cases} H = 4\left(K + \frac{1}{3}G\right)\alpha^2 + 3G - L \\ L = \sqrt{\frac{2}{3}}\tilde{G}_{II}\frac{\partial F}{\partial \gamma^{\mathrm{p}}} = \begin{cases} -\sqrt{\frac{2}{3}}\tilde{G}_{II}h & \text{if } \gamma^{\mathrm{p}} \le \gamma^{\mathrm{p}}_{\mathrm{ult}} \\ 0 & \text{if } \gamma^{\mathrm{p}} > \gamma^{\mathrm{p}}_{\mathrm{ult}} \end{cases} \end{cases} \tag{18}$$

in which τ is the equivalent stress deviator:

$$\tau = \left(\frac{2}{\sqrt{3}}\right)\sqrt{\left(\frac{\sigma_{11}-\sigma_{22}}{2}\right)^2 + \sigma_{12}^2} \tag{19}$$

2.2.2. Constitutive equations for the second-gradient dilation model

Equations (2) and (4) show that the second-gradient model reduces to a second-gradient dilation model if the double stresses satisfy the following conditions:

$$\begin{cases} S_1 = \Sigma_{111} = 2\Sigma_{212} = 2\Sigma_{221} = 2\Sigma_{313} = 2\Sigma_{331} \\ S_2 = \Sigma_{222} = 2\Sigma_{112} = 2\Sigma_{121} = 3\Sigma_{323} = 2\Sigma_{332} \\ S_3 = \Sigma_{333} = 2\Sigma_{113} = 2\Sigma_{131} = 3\Sigma_{223} = 2\Sigma_{232} \\ \Sigma_{122} = \Sigma_{123} = \Sigma_{132} = \Sigma_{133} = 0 \\ \Sigma_{211} = \Sigma_{213} = \Sigma_{231} = \Sigma_{233} = 0 \\ \Sigma_{311} = \Sigma_{312} = \Sigma_{321} = \Sigma_{322} = 0 \end{cases} \tag{20}$$

Consequently, the following equation holds for a kinematically admissible displacement field u_i^*

$$\int_\Omega \left(\Sigma_{ijk} \frac{\partial^2 u_i^*}{\partial x_j \partial x_k} \right) \mathrm{d}V = \int_\Omega \left(S_j \frac{\partial^2 u_i^*}{\partial x_j \partial x_i} \right) \mathrm{d}V \tag{21}$$

Following the framework adopted in the studies of Mindlin, we assume an isotropic linear elastic relationship between the double stresses and the macrovolume change gradient. For a two-dimensional case, Mindlin [15] proved that

$$\begin{bmatrix} \Sigma_{111} \\ \Sigma_{112} \\ \Sigma_{121} \\ \Sigma_{122} \\ \Sigma_{211} \\ \Sigma_{212} \\ \Sigma_{221} \\ \Sigma_{222} \end{bmatrix} = \begin{bmatrix} a_{12345} & 0 & 0 & a_{23} & 0 & a_{12} & a_{12} & 0 \\ 0 & a_{145} & a_{145} & 0 & a_{25} & 0 & 0 & a_{12} \\ 0 & a_{145} & a_{145} & 0 & a_{25} & 0 & 0 & a_{12} \\ a_{23} & 0 & 0 & a_{34} & 0 & a_{25} & a_{25} & 0 \\ 0 & a_{25} & a_{25} & 0 & a_{34} & 0 & 0 & a_{23} \\ a_{12} & 0 & 0 & a_{25} & 0 & a_{145} & a_{145} & 0 \\ a_{12} & 0 & 0 & a_{25} & 0 & a_{145} & a_{145} & 0 \\ 0 & a_{12} & a_{12} & 0 & a_{23} & 0 & 0 & a_{12345} \end{bmatrix} \begin{bmatrix} \chi_{111} \\ \chi_{112} \\ \chi_{121} \\ \chi_{122} \\ \chi_{211} \\ \chi_{212} \\ \chi_{221} \\ \chi_{222} \end{bmatrix} \tag{22}$$

where $\chi_{ijk} = \frac{\partial^2 u_i}{\partial x_j x_k}$, and the constants a_* depend on five parameters a_i $i \in \{1, 2, 3, 4, 5\}$:

$$\begin{cases} a_{12345} = 2(a_1 + a_2 + a_3 + a_4 + a_5) \\ a_{23} = a_2 + 2a_3 \\ a_{12} = a_1 + \frac{a_2}{2} \\ a_{25} = \frac{a_2}{2} + a_5 \\ a_{34} = 2(a_3 + a_4) \end{cases} \tag{23}$$

Using the relationship between the components of the double dilation stresses given by Equation (20), we thus obtain:

$$\begin{cases} a_{12345} = 2a_1 \\ a_{23} = 0 \\ a_{12} = a_1 \\ a_{25} = 0 \\ a_{34} = 0 \end{cases} \quad \begin{bmatrix} \Sigma_{111} \\ \Sigma_{112} \\ \Sigma_{121} \\ \Sigma_{122} \\ \Sigma_{211} \\ \Sigma_{212} \\ \Sigma_{221} \\ \Sigma_{222} \end{bmatrix} = \begin{bmatrix} 2a_1 & 0 & 0 & 0 & 0 & a_1 & a_1 & 0 \\ 0 & \frac{a_1}{2} & \frac{a_1}{2} & 0 & 0 & 0 & 0 & a_1 \\ 0 & \frac{a_1}{2} & \frac{a_1}{2} & 0 & 0 & 0 & 0 & a_1 \\ 0 & 0 & 0 & 0 & 0 & 0 & 0 & 0 \\ 0 & 0 & 0 & 0 & 0 & 0 & 0 & 0 \\ a_1 & 0 & 0 & 0 & 0 & \frac{a_1}{2} & \frac{a_1}{2} & 0 \\ a_1 & 0 & 0 & 0 & 0 & \frac{a_1}{2} & \frac{a_1}{2} & 0 \\ 0 & a_1 & a_1 & 0 & 0 & 0 & 0 & 2a_1 \end{bmatrix} \begin{bmatrix} \chi_{111} \\ \chi_{112} \\ \chi_{121} \\ \chi_{122} \\ \chi_{211} \\ \chi_{212} \\ \chi_{221} \\ \chi_{222} \end{bmatrix} \tag{24}$$

The constitutive equations for the second-gradient dilation model can therefore finally be written as

$$S_j = \beta \frac{\partial \epsilon_V}{\partial x_j} \tag{25}$$

in which $\beta = (n+1)a_1$. n is introduced in order to account for the dimensionality of the problem (i.e. $n = 2$ in a two-dimensional problem and $n = 3$ in a three-dimensional problem). The only additional parameter to be calibrated is β.

Thus, a total of seven material parameters must be defined: six for the underlying Drucker–Prager elastoplastic model, (E, ν, α, σ_Y, h and $\gamma^{\mathrm{p}}_{\mathrm{ult}}$), and only one for the second-gradient component (β).

2.3. Analytical implements

In this section, we present the solution to a simple boundary value problem. For conciseness, we do not provide details of the resolution. The problem considered is a shear band analysis based on the work of Vermeer [35] and has previously been solved using the Mohr–Coulomb classical constitutive equations in a complete local second-gradient model [30], and using the Hujeux classical constitutive equations [36] in a second-gradient dilation model [31]. For this simple analytical problem, we can derive an explicit relationship between the extra parameter, β, which appears in the constitutive equations (Equation (25)), and the implicit internal length of the domain under consideration, denoted by l_c. In the shear band analysis, the orientation of the shear band is known and the stress-state orientation is free. We assume that the existing stress state is homogeneous and search for solution for the rate. We make the following five assumptions:

- An infinite geomaterial layer bounded by two parallel planes at $(x=0)$ and $(x=l)$ is considered. The direction normal to the plane under consideration is denoted by z.
- The plane strain is oriented in the z direction.
- The displacement field is defined by only two components: u along the x-axis and v along the y-axis.
- The components u and v depend only on x. Derivatives with respect to x are denoted by a "$\prime$".
- The rates at the boundaries are known. At $x=0$, $\dot{u}=0$ and $\dot{v}=0$. At $x=l$, $\dot{p}_i$ and $i\in\{1,2\}$ (see Equation (6)) are given. We assume once more that $P_i=0$ (see Equation (6)).

The system of differential equations to be solved can be written in the form of Equation (26). The second equation results in a linear relationship between the components of the displacement field in the shear band.

$$\begin{cases} \dot{u}'''\beta\Lambda^{\mathrm{ep}}_{1212} - \left(\Lambda^{\mathrm{ep}}_{1111}\Lambda^{\mathrm{ep}}_{1212} - \Lambda^{\mathrm{ep}}_{1211}\Lambda^{\mathrm{ep}}_{1112}\right)\dot{u}' = \left(\Lambda^{\mathrm{ep}}_{1112}\dot{p}_2 - \dot{p}_1\Lambda^{\mathrm{ep}}_{1212}\right) \\ \left(\dot{p}_2 - \Lambda^{\mathrm{ep}}_{1211}\dot{u}'\right) = \dot{v}'\Lambda^{\mathrm{ep}}_{1212} \end{cases} \tag{26}$$

The solutions to this set of differential equations depend on the constitutive coefficients, which are themselves dependent on both the stress state and the classical material parameters (see Equation (17)). The general solution to this set of equations is given by:

$$\dot{u}' = \dot{u}'_0 + (C_{21}\cos(\omega x) + C_{22}\sin(\omega x)) \tag{27}$$

where $\omega = \sqrt{\frac{\Lambda^{\mathrm{ep}}_{1211}\Lambda^{\mathrm{ep}}_{1112} - \Lambda^{\mathrm{ep}}_{1212}\Lambda^{\mathrm{ep}}_{1111}}{\beta\Lambda^{\mathrm{ep}}_{1212}}}$, C_{21} and C_{22} are integration constants, and $\dot{u}'_0$ is a particular solution. The solution $\dot{v}'$ is given by Equation (26). The trigonometric functions clearly indicate the appearance of a localised structure. The localised structure in this problem has an internal length $l_c = \frac{2\pi}{\omega}$. The relationship between l_c and β can therefore be deduced according to Equation (28):

$$\frac{\beta}{l_c^2} = \frac{\Lambda^{\mathrm{ep}}_{1112}\Lambda^{\mathrm{ep}}_{1211} - \Lambda^{\mathrm{ep}}_{1111}\Lambda^{\mathrm{ep}}_{1212}}{4\pi^2\Lambda^{\mathrm{ep}}_{1212}} = \frac{-C}{4\pi^2\Lambda^{\mathrm{ep}}_{1212}} \tag{28}$$

Equation (28) depends on the constant C, which is assumed to determine the localisation criterion, i.e. the threshold of the possible localisation. Consequently, this quantity becomes positive as soon as it is possible for localisation to occur in the domain under consideration. Second, this ratio depends only on the first gradient quantities via the elasto-plastic tensor components given by Equation (17). The localisation threshold for the second-gradient model is therefore the same as the localisation threshold in the underlying first gradient model. In practice, this ratio can be obtained from homogeneous computations involving only the classical constitutive equations (see Section 3). Next, we derive β (the additional coefficient) from this ratio.

In examining Equation (28) and assuming that the terms on the right-hand side are known, it is clearly necessary to specify an internal length, l_c, in order to estimate the extra parameter β. Here, we assume that the internal length is equal to the width of the bands that are obtained from the 3D-localisation computations detailed in Section 4. The localised structures in the 3D-applications are therefore assumed to arise and evolve along planes (to be consistent with the assumption of plane strains in the solution to the aforementioned problem). We have no experimental basis for estimating l_c.

l_c can be defined as the grain size of coarse-grained materials such as sand [28]. In these materials, internal length l_c can be estimated from the thickness of the shear bands, $t_s b$, based on a $t_s b/l_c$ ratio of between 15 and 20 [13,23]. As already mentioned, while shear bands can be measured in granular materials with conventional X-ray CT systems, this is not the case for fine-grained rocks such as the shales considered in the present work. Because of a resolution issue, we are unable to measure shear bands and cannot therefore infer an internal length for the material under study, especially given the size of the samples used in the triaxial compression tests. However, measurements of shear bands have been carried out at the European Synchrotron Radiation Facility on smaller samples of claystone [28] and marl [33]. The measured shear-band thicknesses for these materials were about 70 μm and 50 μm, respectively. This compares to a thickness of about 5 mm for a sand tested with the same apparatus and under the same conditions. Measurements performed on a soft clay [37], yielded shear-band thicknesses on the order of 1 mm to 8 mm, depending on the displacement rate applied during triaxial

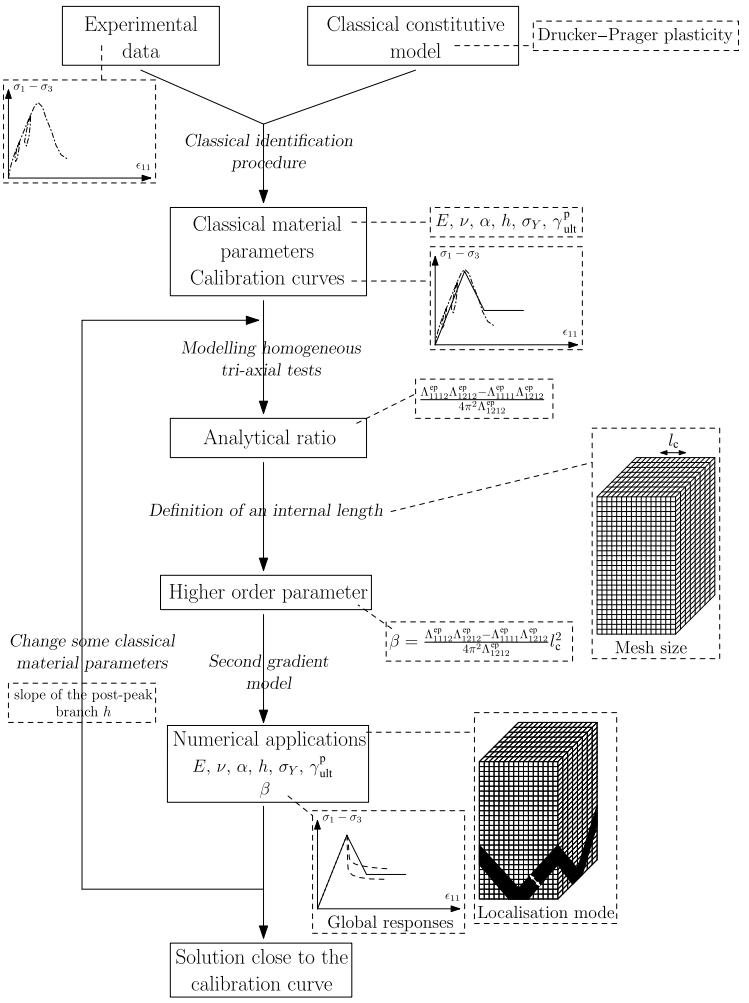

Fig. 2. Flow chart for the method.

compression tests. For these kind of materials, the internal length is proportional to the ratio $\sqrt{\frac{a_1}{|m|}}$, where $|m|$ is the absolute value of the negative slope of the softening branch in the Drucker–Prager model [23].

For simplicity, we considered mesh-size to be a known input and used a minimum of four or five elements for the band width as a rule-of-thumb for obtaining mesh-independent results [29,23]. There is no known method for calibrating the internal length. In the numerical computations detailed in Section 4, the mesh size was chosen with a view to eventually extending the methodology to large-scale industrial applications. For example, for the specimens studied in Section 4, which have a width of approximately 34 mm, an internal length of 10 mm was used to derive β.

3. Methodology

In this section, the numerical calibration method developed in this paper is presented. The method will then be then applied to a shale material in Section 4. The approach can be viewed as a classical identification procedure that integrates the theoretical implements detailed in Section 2.3 in order to calibrate the higher order parameter β. The method is illustrated in the flow chart in Fig. 2.

In general, the material parameters that appear in the classical constitutive equations are calibrated using laboratory tests that are traditionally used to model certain large-scale physical phenomena. The identification procedure is the first step in the process and aims to define the material parameters that appear in the first gradient model. If the constitutive equations used are fairly simple, only standard triaxial compression tests are generally required. However, additional stress paths may be required for more complex models. For the Drucker–Prager constitutive equations, the standard compression paths are sufficient for calibrating the six parameters that appear (E, ν, α, σ_Y, h and $\gamma^{\mathrm{p}}_{\mathrm{ult}}$; see Section 2.2.1). Upon completion of the classical identification procedure, the classical material parameters are then computed. The global numerical responses are identified by the calibration curves, i.e. the global numerical responses that most accurately describe the experimental data.

In the application presented in Section 4, the calibration curves are synonymous with the typical stress-axial strain curves obtained through modelling of traditional triaxial compression tests.

The theoretical implements from Section 2.3 are used in the second step to estimate the only additional coefficient β, that appears in the higher order constitutive equations (see Section 2.2.2). The classical material parameters obtained in the first step and the analytical ratio in the right-hand side of Equation (28) can all be derived from the triaxial compression tests that were modelled in the first step. As discussed in the previous section, the internal length value l_c can be defined from geometrical considerations, including the mesh size and the rule-of-thumb that a minimum of four or five elements be used to determine the shear-band width (see Fig. 2). Consequently, β can be estimated for a given set of classical material parameters and for a given internal length, which is mesh-size dependent. Completion of these first two steps therefore provides values for all of the parameters of the constitutive equations needed to perform the computations.

In the third step, the localisation computational method (i.e. the computations using the first and second-gradient constitutive equations) is validated numerically by modelling a number of heterogeneous triaxial tests. Two types of numerical results are obtained: the localisation modes from investigating a plastic indicator (i.e. the instantaneous plastic state or accumulated plastic shear strains) and the responses in the stress-axial strain plane (Fig. 2). The localisation modes and the responses are then compared to the assumed value of the internal length from the previous step, which was used to estimate β and the calibration curves obtained from the first step of the classical procedure, respectively.

The higher order terms affect the stress–strain relationship, resulting in differences between the global responses obtained from the localisation computations and the calibration curves acquired from the first step. Consequently, if the classical material parameters calibrated in the first step are retained, it is not possible to accurately describe the experimental data in the localisation computations unless very high internal lengths are used (i.e. very high values of β). Such values, however, are not consistent with the mesh size used and some of the classical material parameters must therefore be changed. For the Drucker–Prager constitutive equations and the triaxial global responses, the additional parameter β affects the post-peak branch in the typical stress-axial strain plane. Consequently, it is necessary to change the corresponding classical material parameter that exhibits similar effects, i.e. h (see Section 2.2.1).

The analytical results used to estimate β in the second step depend on the classical material constants that were obtained in the first step. Consequently, changing h to better describe the calibration curves in the localisation computations requires that both the analytical implements and β be recalculated. This, of course, means that the numerical calculations used to validate the method must be performed again.

The method is summarised below.

(i) Complete the classical identification procedure to determine the material parameters that appear in the first gradient model.
(ii) Compute the ratio given by Equation (28) and use the internal length l_c, as defined by geometrical considerations, to estimate the additional parameter β.
(iii) Perform the localisation computations using the parameters derived in steps 1 and 2 above, and compare the global responses and the localised patterns to the calibration curves in step 1 and the assumed internal length, respectively.
(iv) Modify the required classical material parameters (i.e. h) and repeat steps 2 and 3.
(v) Iterate the loop until a solution is found that approximates the calibration curve, i.e. the experimental data.

4. Application to a shale material

To validate the method outlined in Section 3, we applied it to experimental results of triaxial tests performed at the Geo-Ressources Laboratory on porous shale specimens from Sisteron, France. The tests were performed on cylindrical specimens, 38 mm in diameter and 76 mm in height, and were undertaken at confining pressures of 0, 2, 5 and 10 MPa. However, because the results for the post-peak branches were only relevant for the test at 2 MPa, we only used the results of this single test (Fig. 3).

The classical identification procedure (Step 1 of the method), was carried out first, by modelling homogeneous triaxial tests in order to calibrate the Drucker–Prager material parameters, as described below. The localisation computations (Steps 4 and 5) were then performed and are presented in the final section of this paper.

4.1. Classical calibration procedure

The first step of the method is the classical identification procedure. Here, we describe the calibration of the Drucker–Prager material parameters using the experimental data presented in Fig. 3. Six coefficients must be defined (see Section 2.2):

- σ_Y, α, γ^p_{ult}, h in the Drucker–Prager constitutive equations;
- E and ν or G and K for the linear elastic branch.

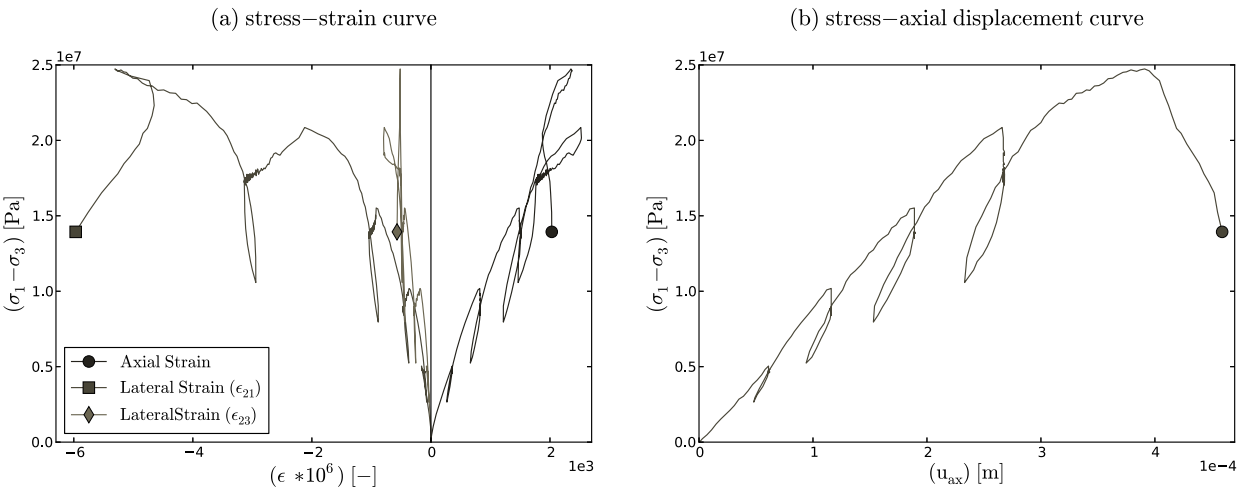

Fig. 3. Working data from triaxial compression tests performed at a confining pressure of 2 MPa.

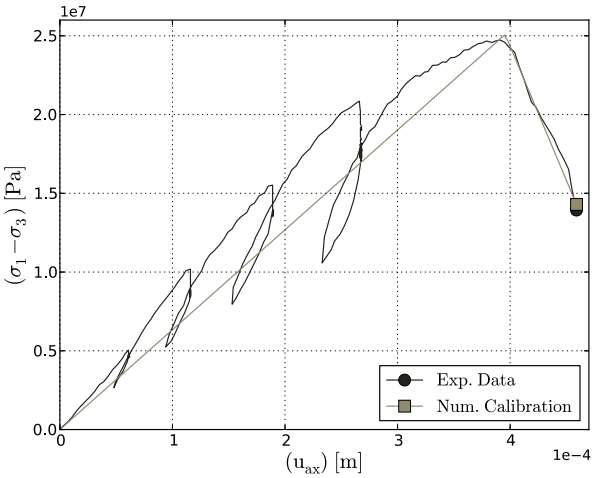

Fig. 4. Calibration of the Drucker–Prager parameters.

Table 1
Drucker–Prager material parameters obtained using the classical identification procedure (Step 1).

E	4.8	GPa	Young's modulus
ν	0.38	–	Poisson's ratio
α	0.31	–	Dilation coefficient
σ_Y	15.4	MPa	Peak stress
h	−1.7	GPa	Post-peak slope
γ^p_{ult}	0.01	–	Residual accumulated plastic strain
C	7	MPa	Cohesion
ϕ	23	°	Friction angle

The elastic parameters are given by the pre-peak branch in Fig. 3(b) (Table 1). The parameters σ_Y and α are equivalent to the Mohr–Coulomb parameters C and ϕ (see Equation (11)), respectively, which are in turn related to the intercept and the slope in the $\{\sigma_3, \sigma_1\}$-plane. The parameter h represents the mean post-peak slope in the stress-axial strain plane.

The calibration was conducted on a material point by modelling the homogeneous triaxial tests. Fig. 4 shows the typical results obtained and the material constants are summarised in Table 1. The curves labelled *Exp.Data* and *Num.Calibration* are the reference experimental curve and numerical calibration curve, respectively.

At low confining pressures, failure in geomaterials is mainly brittle and the critical state (the horizontal plateau in Fig. 1(a)) is therefore rarely reached in triaxial compression tests. Consequently, there is an uncertainty in the γ^p_{ult}, a parameter that was arbitrarily assumed to be 1% in this study.

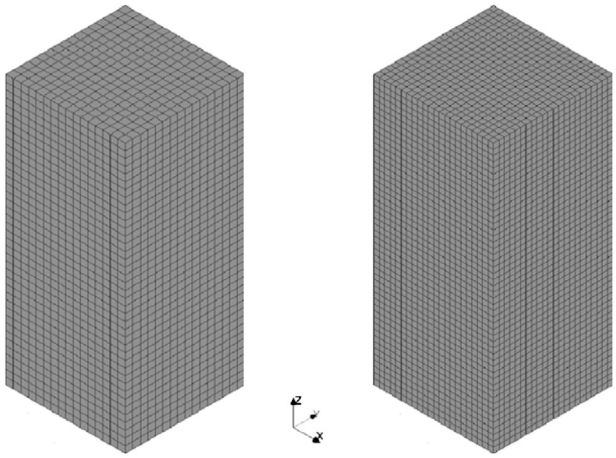

Fig. 5. Structured meshes.

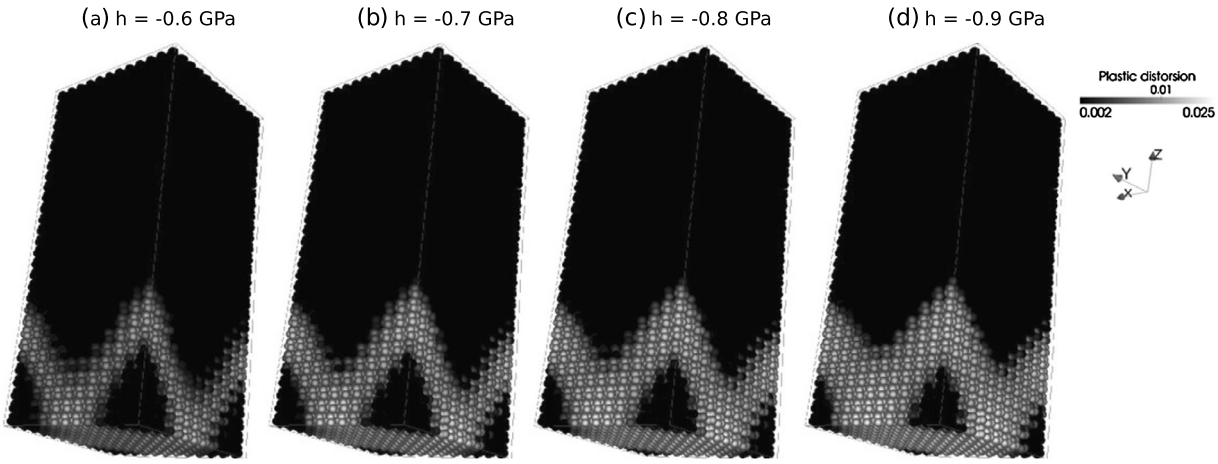

Fig. 6. Distribution of the accumulated plastic shear strain for an axial displacement of −0.41 mm and different values of h.

4.2. Localisation computations

This section addresses the localisation computations that were performed in Steps 4 and 5 (see Section 3) to validate the method. The value of the mesh size (Fig. 5) is used to determine the parameter l_c, which is in turn used to determine the additional parameter β. The parameter l_c remains unchanged while h varies depending on the process, as shown in Fig. 2. Thus, the right-hand side of Equation (28) varies while l_c remains constant.

Difficulties have been encountered in the observation and characterisation of shear bands in cylindrical specimens. These problems are related to the circular symmetries of the cylindrical shapes and are still under debate. Consequently, parallel-piped specimens have been used to model the triaxial test instead. Fig. 5 shows the two structured quadratic meshes that were used in this study. The numerical specimen had the same height as the experimental specimen. The width of the numerical specimen was obtained by equating the area of the cylinder to that of the parallel-piped specimen (i.e. a width of 33.6 mm was obtained for the parallel-piped specimen and a width of 38 mm was obtained for the cylinder). An imperfection was introduced to the bottom of the specimen by slightly reducing (by 0.3%) the value of the parameter α (corresponding to a small reduction in the peak σ_Y) to obtain the same localisation patterns in all of the computations and to initiate the localisation phenomenon (see [23,31,29]).

The input parameter l_c used to estimate β was set at 10 mm (about one-third of the horizontal size of the specimens considered for a minimum width of five elements). The slope of the post-peak branch, h, varied from −0.9 GPa to −0.6 GPa.

Fig. 6 shows maps of the accumulated plastic shear strain (γ^p) for a prescribed displacement of −0.41 mm. The smaller the slope h, the wider the apparent localised bands were. The global responses in Fig. 7 clearly show that the strain localisation occurred before the prescribed displacement of −0.41 mm for values of h below −0.6 GPa. Because of the associated plastic flow, the volumetric strains continued to increase even once the critical state had been reached. The width of the localised bands also continued to increase because the regularising effects are related to volume changes.

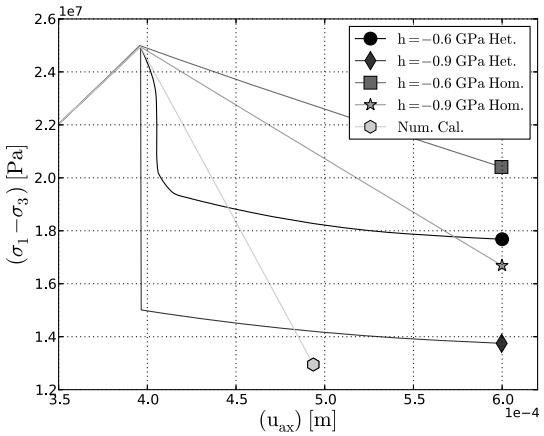

Fig. 7. Global responses in the stress-axial displacement plane for different values of h.

Nevertheless, the band width was fairly consistent with the internal length for the three highest values of h. Note that the localisation occurred along the planes, as predicted by the assumptions used to estimate β.

Fig. 7 illustrates the global responses in the stress-axial displacement plane. The curves labelled *Hom.* correspond to the homogeneous solutions (i.e. the first gradient model and the homogeneous material) and the curves labelled *Het.* represent the localised solutions (i.e. the second gradient model and the material containing an imperfection). The curve labelled *Num.Cal.* is the calibration curve. These results clearly show that the heterogeneous responses differed from those obtained for the homogeneous computations. Values of h below -0.9 GPa did not produce converged solutions. Consequently, h, which affects the post-peak branch, was modified in the localisation computations. As we have reiterated throughout this paper, the need to modify the parameters reflects the inadequacy of the classical calibration procedure for computations of higher order continuum methods. An appropriate procedure should be developed that will allow the additional coefficients to be estimated from experimental data. Finally, before localisation (i.e. before the abrupt decrease in stress), the improved fit with the calibration curve produced $h = -0.6$ GPa (see Fig. 7).

In Fig. 7, the calibration curve from Fig. 4 is superimposed on the experimental curve, revealing the close agreement between the modelled and experimental results. A better fit of second-gradient modelling with experimental curves might be obtained by using a constitutive law that is more complex and rich than the Drucker–Prager law, for example the L& K model (see [24]). Finally, it should be noted that both meshes shown in Fig. 5 yielded the same results for the second-gradient modelling, thus highlighting the mesh independency of the model.

5. Conclusion and future work

In this paper, a numerical procedure was developed to identify the material parameters that appear in second gradient models. While work remains to be done, the combination of modelling traditional tests and analytical implements provided a simple solution to the problems encountered in calibrating additional coefficients. To validate the approach and clarify various issues, the procedure should in the future be applied to other classical constitutive models (e.g., the L&K constitutive model [24,38]) and other specimen shapes. Results obtained on a cylindrical specimen clearly show that localisation is not as clear-cut with cylindrical shapes as it is with parallel-piped specimens. However, a better fit was obtained for the global responses using a calibration curve defined at a material point. Future research might include study of the solutions uniqueness and extension of the procedure to large-scale cases using more classical methods, such as remeshing.

References

[1] P. Bésuelle, J. Desrue, S. Raynaud, Experimental characterisation of the localisation phenomenon inside a Vosges sandstone in a tri-axial cell, Int. J. Rock Mech. Min. Sci. 37 (2000) 1223–1237.
[2] S.A. Hall, J. Desrues, G. Viggiani, P. Bésuelle, E. Andò, Experimental characterisation of (localised) deformation phenomena in granular geomaterials from sample down to inter- and intra-grain scales, Proc. IUTAM 4 (2012) 54–65.
[3] Z.P. Bazant, et al., Continuum theory for strain softening, J. Eng. Mech. 110 (1984) 1666–1692.
[4] S. Forest, E. Lorrentz, Localization and regularization, in: J. Besson (Ed.), Local Approach to Fracture, Presses de l'École des mines de Paris, Paris, 2004.
[5] G. Pijaudier-Cabot, Z.P. Bažant, Nonlocal damage theory, J. Eng. Mech. 113 (1987) 1512–1533.
[6] J.R. Rice, The localization of plastic deformation, in: W.D. Koiter (Ed.), International Congress of Theoretical and Applied Mechanics, North-Holland, Amsterdam, 1976.
[7] J.W. Rudnicki, J.R. Rice, Conditions for the localisation of the deformation in pressure sensitive dilatant materials, J. Mech. Phys. Solids 23 (1975) 371–394.
[8] I. Vardoulakis, J. Sulem, Bifurcation Analysis in Geomechanics, Blackie Academic and Professional, Glasgow, 1995.
[9] E. Aifantis, On a microstructural origin of certain inelastic models, J. Eng. Mater. Technol. 106 (1984) 326–330.
[10] H. Zbib, E. Aifantis, On the localisation and post localisation of plastic deformation. Part I. On the initiation of shear bands, Res. Mech. 23 (1988) 261–277.

[11] H. Zbib, E. Aifantis, On the localisation and post localisation of plastic deformation. Part II. On the evolution and thickness of shear bands, Res. Mech. 23 (1988) 279–292.
[12] R. de Borst, H. Muhlhaus, Gradient dependant plasticity: formulation and algorithmic aspects, Int. J. Numer. Methods Eng. 35 (1992) 521–539.
[13] I. Vardoulakis, E. Aifantis, A gradient flow theory of plasticity for granular materials, Acta Mech. 87 (1991) 197–217.
[14] P. Germain, La méthode des puissances virtuelles en mécanique des milieux continus: première partie: théorie du second-gradient, J. Méc. 12 (1973) 235–274.
[15] R.D. Mindlin, Second gradient of strain and surface-tension in linear elasticity, Int. J. Solids Struct. 1 (1965) 417–738.
[16] R.D. Mindlin, Micro-structure in linear elasticity, Arch. Ration. Mech. Anal. 16 (1964) 51–78.
[17] R. Chambon, D. Caillerie, N. Hassan, One-dimensional localisation studied with a second grade model, Eur. J. Mech. A, Solids 17 (1998) 637–656.
[18] R. Chambon, S. Crochepeyre, R. Charlier, An algorithm and a method to search bifurcation points in nonlinear problems, Int. J. Numer. Methods Eng. 51 (2001) 315–332.
[19] F. Laigle, Modèle conceptuel pour le développement de lois de comportement adaptées à la conception des ouvrages souterrains, PhD thesis, Laboratoire de tribologie et dynamique des systèmes (LTDS) de l'École centrale de Lyon, Lyon, France, 2004, 353 p.
[20] J. Desrues, R. Chambon, M. Mokni, F. Mazerolle, Void ratio evolution inside shear bands in triaxial sand specimens studied by computed tomography, Gotechnique 46 (1996) 529–546.
[21] E.M. Charalampidou, S.A. Hall, S. Stanchits, H. Lewis, C. Viggiani, Characterization of shear and compaction bands in a porous sandstone deformed under tri-axial compression, Tectonophysics 503 (2011) 8–17.
[22] S. Forest, R. Sievert, Non linear microstrain theories, Int. J. Solids Struct. 43 (2006) 7224–7245.
[23] R. Fernandes, C. Chavant, R. Chambon, A simplified second gradient model for dilatant materials: theory and implementation, Int. J. Solids Struct. 45 (2008) 5289–5307.
[24] R. Plassart, R. Fernandes, A. Giraud, H. Dashnor, F. Laigle, Hydromechanical modelling of an excavation in an underground research laboratory with an elastoviscoplastic behaviour law and regularization by second-gradient of dilation, Int. J. Rock Mech. Min. Sci. 58 (2013) 23–33.
[25] Y. Jia, H.B. Bian, K. Su, D. Kondo, J.F. Shao, Elastoplastic damage modelling of desaturation and resaturation in argillites, Int. J. Numer. Anal. Methods Geomech. 34 (2) (2009) 187–220.
[26] H. Zhou, Y. Jia, J.F. Shao, A unified elastic-plastic and viscoplastic damage model for quasi-brittle rocks, Int. J. Rock Mech. Min. Sci. 45 (8) (2008) 1237–1251.
[27] J. Desrues, Experimental characterization of localized deformation in geomaterials, Lect. Notes Appl. Comput. Mech. 13 (2003) 77–106.
[28] G. Viggiani, Mechanisms of localized deformation in geomaterials: an experimental insight using full-field measurement techniques, in: D. Kolymbas, G. Viggiani (Eds.), Mechanics of Natural Solids, Springer, Berlin, 2009, pp. 105–125.
[29] T. Matsushima, R. Chambon, D. Caillerie, Large strain finite element analysis of local second-gradient models, application to localization, Int. J. Numer. Methods Eng. 54 (2002) 499–521.
[30] R. Chambon, D. Caillerie, R. Matsushima, Plastic continuum with microstructure, local second-gradient theories for geomaterials: localization studies, Int. J. Solids Struct. 38 (2001) 8503–8527.
[31] A. Foucault, Modélisation du comportement cyclique des ouvrages en terre intégrant des techniques de régularisation, PhD thesis, École centrale de Paris, Paris, 2010.
[32] Code_Aster, http://www.code-aster.org.
[33] G. Viggiani, N. Lenoir, P. Bsuelle, M. Di Michiel, S. Marello, J. Desrues, M. Kretzschmer, X-ray microtomography for studying localized deformation in fine-grained geomaterials under triaxial compression, C. R. Mecanique 332 (2004) 819–826.
[34] D.C. Drucker, W. Prager, Soil mechanics and plastic analysis design, Q. J. Mech. Appl. Math. 10 (1952) 157–165.
[35] P. Vermeer, A simple shear band analysis using compliances, in: IUTAM Conf. Def. Fail. Gran. Media, Delft, The Netherlands, 1982.
[36] J.-C. Hujeux, Une loi de comportement pour le chargement cyclique des sols, in: V. Davidovici (Ed.), Génie parasismique, Presses ENPC, Paris, France, 1985, pp. 278–302.
[37] A.S. Gylland, H.P. Jostad, S. Nordal, Experimental study of strain localization in sensitive clays, Acta Geotech. 9 (2014) 227–240.
[38] A. Kleine, Modélisation numérique du comportement des ouvrages souterrains par une approche viscoplastique, PhD thesis, Institut national polytechnique de Lorraine, Nancy, France, 2007.